

**Electron-Ion Recombination Rate Coefficients and  
Photoionization Cross Sections for Astrophysically Abundant  
Elements. VII. Relativistic calculations for O VI and O VII for  
UV and X-ray modeling**

Sultana N. Nahar and Anil K. Pradhan

Department of Astronomy, The Ohio State University, Columbus, OH 43210

Received 2000; accepted \_\_\_\_\_

Submitted to *Astrophys. J. Suppl.*, 2000

arXiv:astro-ph/0304204v1 10 Apr 2003

## ABSTRACT

Aimed at ionization balance and spectral analysis of UV and X-ray sources, we present self-consistent sets of photoionization cross sections, recombination cross sections, and rate coefficients for Li-like O VI and He-like O VII. Relativistic fine structure is considered through the Breit-Pauli R-matrix (BPRM) method in the close coupling approximation, implementing the unified treatment for total electron-ion recombination subsuming both radiative and di-electronic recombination processes. Self-consistency is ensured by using an identical wavefunction expansion for the inverse processes of photoionization and photo-recombination. Radiation damping of resonances, important for H-like and He-like core ions, is included. Compared to previous LS coupling results without radiative decay of low- $n$  ( $n \leq 10$ ) resonances, the presents results show significant reduction in O VI recombination rates at high temperatures. In addition to the total rates, level-specific photoionization cross sections and recombination rates are presented for all fine structure levels  $n$  ( $\ell$  SLJ) up to  $n \leq 10$ , to enable accurate computation of recombination-cascade matrices and spectral formation of prominent UV and X-ray lines such as the 1032,1038 Å doublet of O VI, and the ‘triplet’ forbidden, intercombination, and resonance X-ray lines of O VII at 22.1, 21.8, and 21.6 Å respectively. Altogether, atomic parameters for 98 levels of O VI and 116 fine structure levels of O VII are theoretically computed. These data should provide a reasonably complete set of photoionization and recombination rates in collisional or radiative equilibrium.

*Subject headings:* atomic data — atomic processes — photoionization, dielectronic recombination, unified electron-ion recombination — X-rays: general — line:formation

## 1. INTRODUCTION

Li-like and He-like Oxygen are among the most important atomic species in UV and X-ray plasma diagnostics of astrophysical sources. For example, there is considerable current interest in O VI and O VII as a possible reservoir of ‘missing baryons’ in the warm/hot intergalactic medium in the present universe (Cen et al. 2001, Fang and Canizares 2000, Yoshikawa et al. 2003). In addition to global ionization balance models that require O VI/O VII photoionization and recombination rates, specific spectroscopic diagnostics of both of these ions are related in an interesting but intricate manner. Outflows observed from the ‘warm absorber’ in active galactic nuclei exhibit absorption/emission lines in the X-ray from KLL resonant photoabsorption in O VI, and excitation/recombination of O VII lines. This phenomenon was investigated theoretically by Pradhan (2000) who pointed out that the observed spectra of the well known AGN NGC 5548 shows these features (Kaastra et al. 2000). Recently Arav et al. (2003) have further pursued this suggestion to infer large discrepancies in the UV and X-ray O VI column densities in the outflow from NGC 5548. Ionization balance and spectral formation of O VI and O VII are crucial factors in all such studies.

The inverse atomic processes of photoionization and electron-ion photorecombination of Li-like and He-like ions are also of particular interest in X-ray astronomy to analyze new observations by space based observatories such as the Chandra X-ray Observatory and XMM-Newton, at photon energies and temperatures prevalent in high-temperature sources such as AGB, supernova remnants, hot stellar coronae etc. (e.g. Canizares et al. 2000, in Proceedings of the NASA workshop on *Atomic data needs in X-ray astronomy* 2000). X-ray emission in the  $K\alpha$  complex comprising of the ‘triplet’ feature of resonance (w), intercombination (x,y), and forbidden (z) lines in He-like ions, corresponding to the 4 transitions from the  $n = 2$  levels to the ground

level  $1s^2 (^1S_0) \leftarrow 1s2p(^1P_1^o), 1s2p(^3P_{2,1}^o), 1s2s(^3S_1)$  respectively, yields valuable spectral diagnostics of temperature, density, ionization balance, and abundances in the plasma source. Calculations of the recombination-cascade contributions for these important lines requires accurate atomic parameters for fine structure levels up to fairly high  $n$  levels, as presented in this report.

In the Present work we report new results for self-consistent data sets for photoionization and recombination for  $(e + O V) \rightarrow O VI$  and  $(e + O VI) \rightarrow O VII$ , using a unified theoretical method that takes account of both radiative and di-electronic recombination processes (RR and DR). Although treated separately in other previous treatments, both recombination processes, RR and DR, are inseparable in nature. A unified treatment is therefore not only theoretically and computationally more accurate, it is also more practically convenient for applications since a single recombination rate coefficient takes account of both RR and DR in an ab initio manner. For highly charged ions it is important to consider relativistic fine structure explicitly in the theoretical formulation, in addition to the electron correlation effects. Previous results for O VI (Nahar 1998, 1999) were obtained in a non-relativistic LS coupling approximation; relativistic effects were partially included for O VII. To further improve the accuracy, as well as to provide extensive sets of data for astrophysical models, we have re-calculated all photoionization cross sections, electron-ion recombination cross sections, and rate coefficients using the relativistic Breit-Pauli R-matrix (BPRM) method. Similar calculations have previously been reported for He- and Li-like ions C V and C IV (Nahar et al. 2000), and Fe XXV and Fe XXV (Nahar et al. 2001).

## 2. THEORY

The unified method of electron-ion recombination (Nahar and Pradhan 1992) yields self-consistent sets of atomic parameters for photoionization and recombination for atoms

and ions (e.g. Nahar and Pradhan 1997, Paper I of this series). Relativistic extension using the BPRM method is described in Zhang and Pradhan (1997), Pradhan and Zhang (1997) and Zhang et al. (1999). Photorecombination of an incident electron with the target ion may occur through (i) non-resonant, background continuum, or radiative recombination (RR),

$$e + X^{++} \rightarrow h\nu + X^+, \quad (1)$$

which is the inverse process of direct photoionization, or (ii) through a two-step recombination process via autoionizing resonances, i.e. dielectronic recombination (DR):

$$e + X^{++} \rightarrow (X^+)^{**} \rightarrow \begin{cases} (i) e + X^{++} \\ (ii) h\nu + X^+ \end{cases}, \quad (2)$$

where the quasi-bound doubly-excited autoionizing state may lead either to (i) autoionization, a radiation-less transition to a lower target state with the electron going into a continuum, or (ii) radiative stabilization to a recombined bound state via decay of the ion core (usually to the ground state) with the electron captured.

The extension of the R-matrix method to electron-ion recombination calculations entails close coupling calculations for photoionization and electron-ion scattering. Identical eigenfunction expansion for the target (core) ion is employed for both processes, enabling inherently self-consistent results in an ab initio manner for a given ion. We consider photoionization from, and recombination into, the infinity of levels of the (e + ion) system. These are divided into two groups of bound levels: (A) with  $\nu \leq \nu_o$  and all possible fine structure  $J\pi$  symmetries, and (B)  $\nu_o < \nu \leq \infty$ ; where  $\nu$  is the effective quantum number relative to the target threshold(s). Photoionization and recombination calculations are carried out in detail for all group A levels, while group (B) levels are treated through quantum defect theory of DR within close the coupling approximation (Bell and Seaton 1985, Nahar and Pradhan 1994). A generally valid approximation made in recombination

to group (B) levels is that the background contribution is negligible, and DR is the dominant process in the region below the threshold of convergence for high- $n$  resonances.

In the close coupling (CC) approximation the target ion (core) is represented by an  $N$ -electron system. The total wavefunction,  $\Psi(E)$ , of the  $(N+1)$  electron-ion system of symmetry  $J\pi$  is represented in terms of an expansion of target eigenfunctions as:

$$\Psi(E) = A \sum_i \chi_i \theta_i + \sum_j c_j \Phi_j, \quad (3)$$

where  $\chi_i$  is the target wavefunction in a specific level  $J_i\pi_i$  and  $\theta_i$  is the wavefunction for the  $(N+1)$ -th electron in a channel labeled as  $S_iL_i(J_i)\pi_i k_i^2 \ell_i(J\pi)$ ;  $k_i^2$  being its incident kinetic energy.  $\Phi_j$ 's are the correlation functions of the  $(N+1)$ -electron system that account for short range correlation and the orthogonality between the continuum and the bound orbitals. In relativistic BPRM calculations the set of  $SL\pi$  are recoupled for  $J\pi$  levels of (e + ion)-system, followed by diagonalisation of the Hamiltonian,

$$H_{N+1}^{BP} \Psi = E \Psi, \quad (4)$$

where the BP Hamiltonian is

$$H_{N+1}^{BP} = H_{N+1}^{NR} + H_{N+1}^{\text{mass}} + H_{N+1}^{\text{Dar}} + H_{N+1}^{\text{so}}. \quad (5)$$

The first term,  $H_{N+1}^{NR}$ , is the nonrelativistic Hamiltonian,

$$H_{N+1}^{NR} = \sum_{i=1}^{N+1} \left\{ -\nabla_i^2 - \frac{2Z}{r_i} + \sum_{j>i}^{N+1} \frac{2}{r_{ij}} \right\}, \quad (6)$$

and the additional one-body terms are the mass correction term,  $H^{\text{mass}} = -\frac{\alpha^2}{4} \sum_i p_i^4$ , the Darwin term,  $H^{\text{Dar}} = \frac{Z\alpha^2}{4} \sum_i \nabla^2(\frac{1}{r_i})$ . and the spin-orbit interaction term,  $H^{\text{so}} = Z\alpha^2 \sum_i \frac{1}{r_i^3} \mathbf{l}_i \cdot \mathbf{s}_i$ , respectively.

The positive and negative energy states (Eq. 4) define continuum or bound (e + ion) states, such that,  $E = k^2 > 0$  for continuum (scattering) channels and  $E = -\frac{z^2}{\nu^2} < 0$

for bound states, where  $\nu$  is the effective quantum number relative to the core level. If  $E < 0$  then all continuum channels are ‘closed’ and the solutions represent bound states. The matrix element for the bound-free transition,  $\langle \Psi_B || \mathbf{D} || \Psi_F \rangle$ , can be obtained from the continuum wavefunction ( $\Psi_F$ ) and the bound wavefunction ( $\langle \Psi_B$ ).  $\mathbf{D}$  is the dipole operator,  $\mathbf{D}_L = \sum_i r_i$ , in length form and  $\mathbf{D}_V = -2 \sum_i \Delta_i$  in velocity form, the sum being the number of electrons.

Photoionization cross sections of all possible states with  $n \leq n_{\max} \sim 10$  – are obtained as in the CC approximation as in the Opacity Project (Seaton 1987, *The Opacity Project* 1995, 1996), extended to include the relativistic effects under the Iron Project (Hummer et al. 1993). The photoionization cross section is obtained as

$$\sigma_{PI} = \frac{1}{g} \frac{4\pi^2}{3c} \omega \mathbf{S}, \quad (7)$$

where  $g$  is the statistical weight factor of the bound state and  $\mathbf{S}$  is the dipole line strength,  $\mathbf{S} = |\langle \Psi_B || \mathbf{D} || \Psi_F \rangle|^2$ . For highly charged H- and the He-like ions, the probability of radiation decay of an autoionizing state is usually comparable to that of autoionization as discussed in Nahar et al. (2000). With strong dipole allowed  $2p \rightarrow 1s$  and  $1s2p$  ( $^1P_1^o$ )  $\rightarrow 1s^2$  ( $^1S_0$ ) transitions autoionizing resonances are radiatively damped to a significant extent. The radiative damping effect of all near-threshold resonances, up to  $\nu \leq 10$ , is included using a resonance fitting procedure (Sakimoto et al. 1990, Pradhan and Zhang 1997, Zhang et al. 1999).

The photo-recombination cross section,  $\sigma_{RC}$ , is related to photoionization cross section,  $\sigma_{PI}$ , through principle of detailed balance (Milne relation) as

$$\sigma_{RC}(\epsilon) = \frac{\alpha^2}{4} \frac{g_i}{g_j} \frac{(\epsilon + I)^2}{\epsilon} \sigma_{PI} \quad (8)$$

in Rydberg units;  $\alpha$  is the fine structure constant,  $\epsilon$  is the photoelectron energy, and  $I$  is the ionization potential.  $\sigma_{RC}$  are computed from the photoionization cross sections

at a sufficiently large number of energies to delineate the non-resonant background and the autoionizing resonances, thereby representing both radiative and the dielectronic recombination (RR and DR) processes. In the unified treatment the photoionization cross sections,  $\sigma_{\text{PI}}$ , of a large number of low- $n$  bound states – all possible states with  $n \leq n_{\text{max}} \sim 10$  – are obtained as described above. It is assumed that the recombining ion is in the ground state, and recombination can take place into the ground or any of the excited recombined (e+ion) states.

Recombination rate coefficients of individual levels are obtained by convolving recombination cross sections over Maxwellian electron distribution  $f(v)$  at a given temperature,

$$\alpha_{RC}(T) = \int_0^\infty v f(v) \sigma_{RC} dv. \quad (9)$$

Contribution of these low- $n$  group (A) bound states to the total  $\sigma_{RC}$  is obtained by summing over all low- $n$  group (A) states.  $\sigma_{RC}$  thus obtained from  $\sigma_{\text{PI}}$ , including the radiatively damped autoionizing resonances (Eq. (8)), corresponds to the total (DR+RR) unified recombination cross section.

Recombination into the high- $n$  states,  $n_{\text{max}} < n \leq \infty$ , (Fig. 1 of Nahar & Pradhan 1994) are included separately. To each excited threshold of the core,  $J_i \pi_i$ , belongs an infinite series of  $(N+1)$ -electron levels,  $J_i \pi_i \nu \ell$ , to which recombination can occur. For the high  $\nu$  levels DR dominates while the background RR is negligibly small. The contributions from these levels are added by calculating the DR collision strengths,  $\Omega_{\text{DR}}$ , employing the precise theory of radiation damping by Bell and Seaton (1985; Nahar & Pradhan 1994). The recombination cross section,  $\sigma_{RC}$  in Megabarns (Mb), is related to the collision strength,  $\Omega_{\text{RC}}$ , as

$$\sigma_{RC}(i \rightarrow j)(Mb) = \pi \Omega_{RC}(i, j) / (g_i k_i^2) (a_o^2 / 1. \times 10^{-18}), \quad (10)$$

where  $k_i^2$  is the incident electron energy in Rydbergs. As  $\sigma_{RC}$  diverges at zero-photoelectron



energy, the total collision strength,  $\Omega$ , is used in the recombination rate calculations. Background photoionization cross sections for the high- $n$  group (B) levels are computed hydrogenically, which is referred to as the “high- $n$  top-up” (Nahar 1996).

### 3. COMPUTATIONS

Relativistic BPRM calculations in intermediate coupling are carried out in the close coupling approximation using the  $R$ -matrix package of codes. These codes are extensions of the Opacity Project codes (Berrington et al. 1987) to include relativistic effects (Scott & Burke 1980, Scott & Taylor 1982, Berrington et al. 1995), as implemented under the Iron Project (Hummer et al. 1993). The calculations span several stages of computation using one-electron orbital wavefunctions for the core or target ion from an updated version of the atomic structure code SUPERSTRUCTURE, using a scaled Thomas-Fermi-Dirac potential (Eissner et al. 1974).

The wavefunction expansion for O VI consists of 17 fine structure levels of configurations  $1s^2$ ,  $1s2s$ ,  $1s2p$ ,  $1s3s$ ,  $1s3p$ , and  $1s3d$  of O VII. The levels, along with their relative energies, are given in Table 1. The set of correlation configurations in the atomic structure calculations and the Thomas-Fermi scaling parameter ( $\lambda_{nl}$ ) for each orbital are also given in Table 1. The second term in Eq. (3), with bound state correlation functions for O VI, includes all possible  $(N + 1)$ -particle configurations with 0 to maximum orbital occupancies:  $2s^2$ ,  $2p^2$ ,  $3s^2$ ,  $3p^2$ ,  $3d^2$ ,  $4s$  and  $4p$ .

For O VII, the wavefunction expansion consists of 16 fine structure levels of O VIII of  $1s$ ,  $2s$ ,  $2p$ ,  $3s$ ,  $3p$ ,  $3d$ ,  $4s$ ,  $4p$ ,  $4d$  and  $4f$ , as given in Table 1. The bound state correlation functions included all configurations from 0 to maximum orbital occupancies:  $1s^2$ ,  $2s^2$ ,  $2p^2$ ,  $3s^2$ ,  $3p^2$ ,  $3d^2$ ,  $4s^2$  and  $4p^2$ ,  $4d$  and  $4f$ . The energies in Table 1 are observed values (from the NIST website: [www.nist.gov](http://www.nist.gov)). Although calculated energies are less than one percent of the

observed ones, the latter are used in the computations to obtain more accurate positions of resonances. Radial integrals for the partial wave expansion in Eq. 3 are specified for orbitals  $0 \leq \ell \leq 9$ , with a R-matrix basis set 40 ‘continuum’ functions (NRANG2) for O VI, and 30 for O VII.

Both the *partial* and the *total* photoionization cross sections are obtained for all bound levels. Coupled channel calculations for  $\sigma_{\text{PI}}$  include both the background and the resonance structures (due to the doubly excited autoionizing states) in the cross sections. Radiation damping of resonances up to  $n = 10$  are included through use of the extended codes STGF and STGBF (Nahar and Pradhan 1994, Zhang et al. 1999). The BPRM calculations are carried out for each total angular momentum symmetry  $J\pi$ , corresponding to a set of fine structure target levels  $J_t$ . Radiation damping of resonances within the close coupling BPRM calculations are described in Zhang et al. (1999, and references therein). The program PBRRAD is used to extend the *total* photoionization cross sections in the high energy region, beyond the highest target threshold in the close coupling wavefunction expansion of the ion, by a ‘tail’ using Kramers formula  $\sigma_{\text{PI}}(E) = \sigma_{\text{PI}}^o(E^o/E)^3$  where  $E^o$  is the last tabulated energy above all target thresholds.

Level-specific recombination cross sections  $\sigma_{\text{RC}}(i)$ , into bound levels  $i \equiv n$  (SLJ) of the recombined (e + ion) system, are obtained from *partial* photoionization cross sections  $\sigma_{\text{PI}}(i, g)$  of the level  $i$  into the ground level  $g$  of the recombining ion. These detailed photo-recombination cross sections are calculated in the energy region from the threshold energy up to  $E(\nu = \nu_o \approx 10.0)$ , where  $\nu$  is the effective quantum number relative to the target level of the recombining ion. The resonances up to  $\nu \leq \nu_o$  are delineated with a fine energy mesh. The electrons in this energy range generally recombine to a large number of final (e + ion) levels. Recombination cross sections are computed for all coupled symmetries and levels, and summed to obtain the total  $\sigma_{\text{RC}}$ . Level specific recombination

rate coefficients are obtained using a new computer program, BPRRC (Nahar et al 2000). The level specific rates are obtained for energies going up to infinity. These rates include both non-resonant and resonant contributions up to energies  $z^2/\nu_o^2$ ; Contributions from all autoionizing resonances up to  $\nu \leq \nu_o \approx 10$  are included.

In the higher energy region,  $\nu_o < \nu < \infty$ , below each target threshold where the resonances are narrow and dense and the background is negligible, we compute detailed and resonance averaged DR cross sections. The BPRM DR collision strengths are obtained using extensions of the  $R$ -matrix asymptotic region code STGF (Nahar & Pradhan 1994, Zhang et al. 1999). It is necessary to use a very fine energy mesh in order to delineate the resonance structures.

The program BPRRC sums up the level specific rates, which is added to the contributions from the resonant high- $n$  DR, from resonances with  $\nu_o < \nu < \infty$ , to obtain total recombination rates. As an additional check on the numerical calculations, the total recombination rate coefficients,  $\alpha_R$ , are also calculated from the total recombination collision strength,  $\Omega_{RC}$ , obtained from all the photoionization cross sections, and the DR collision strengths. The agreement between the two numerical approaches is within a few percent.

Finally, the small background (non-resonant) contribution from the high- $n$  states ( $10 < n \leq \infty$ ) to total recombination is also included as the "top-up" part, computed in the hydrogenic approximation (Nahar 1996). This contribution is important at low temperatures, but negligible at high temperatures. At low temperature, recombination rate is dominated by the RR into the infinite number of high- $n$  states, as electron energies are not usually high enough for resonant excitations and DR, and causes a rapid rise in  $\alpha_R(T)$  towards low temperatures.

## 4. RESULTS AND DISCUSSION

Results are presented for photoionization and recombination of O VIII + e  $\rightarrow$  O VI, and O VIII + e  $\rightarrow$  O VII. Odd and even parity energy levels  $n$  (SLJ) of total angular momentum symmetries  $1/2 \leq J \leq 17/2$  are considered for O VI, and  $0 \leq J \leq 4$  for O VII, all bound levels with  $n \leq 10$ .

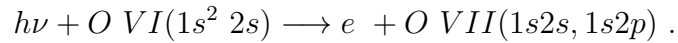
Photoionization cross sections  $\sigma_{PI}$  include both the *total* cross section, leaving the core (residual) ion in the ground and excited levels, as well as the *partial* cross sections, leaving the core ion in the ground level only. The total cross sections are needed in astrophysical applications, such as in ionization balance calculations while parital cross sections are needed for applications such as for recombination rate coefficients. (Both the total and the partial cross sections are available electronically.)

Level-specific and total recombination rate coefficients using the BPRM unified treatment,  $\alpha_i$  ( $n$  SLJ,  $n \leq 10$ ) and  $\alpha_{RC}(T)$  respectively, are presented for O VI and O VII. In the following subsections we describe salient features pertaining to  $\alpha_{RC}(T)$  in numerical form and in figures. Total  $\alpha_{RC}(T)$  are computed two different ways to enable numerical checks: (i) from the sum of the level-specific rate coefficients and the high- $n$  DR contribution, and (ii) from total collision strengths calculated from photoionization cross sections directly, and the DR contribution. The differences between the two are typically within a few percent, thus providing a numerical and self-consistency check particularly on the resolution of resonances. We also present total recombination rate coefficients for the hydrogenic ion O VIII for completeness.

### 4.1. O VI

#### 4.1.1. Photoionization

Figs. 1(a) and (b) show the ground state photoionization cross section for O VI ( $1s^2 2s^2 S_{1/2}$ ). The top panel (a) presents the total photoionization cross section summed over the various target thresholds for ionization, and the bottom panel (b) presents the partial cross sections of the ground level into the ground  $1s^2(^1S)$  level of residual ion O VII. The resonances at high energies belong to Rydberg series converging  $n = 2, 3$  levels. These are the well known KLL, KLn ( $n > 2$ ) as, for example, discussed by Pradhan (2000) and Nahar et al. (2001). Since the first excited levels of  $n=2$  thresholds of the core ion O VII lie at high energies, the cross sections decrease monotonically over a large energy range before the Rydberg series of resonances appears. The total and the partial cross sections are identical below the first excited level of the residual ion beyond which total  $\sigma_{PI}$  increases due to added contributions from excited channels, as shown in the figures. A distinct difference between the total and partial cross sections Fig. 1 comes from the contribution of channels with excited  $n=2$  thresholds. The K-shell ionization jump at the  $n = 2$  target levels in total  $\sigma_{PI}$  is due to inner-shell photoionization:



In X-ray photoionization models inner-shell edges play an important role in overall ionization rates.

Fig. 2 presents partial photoionization cross sections of the Rydberg series of levels  $1s^2 ns$ ,  $2 \leq n \leq 10$ . As noted in earlier works, photoionization cross section of Rydberg levels exhibit wide resonances known as photoexcitation-of-core (PEC) resonances at energies associated with dipole transitions in the core ion. We see such PEC resonances in in cross sections of all bound levels of O VI, as in Fig. 2 at photon energies 41.788, 42.184, 48.804 and 48.922 Ry due to core excitations to levels  $1s2p(^3P_1^o)$ ,  $1s2p(^1P_1^o)$ ,  $1s3p(^3P_1^o)$ , and  $1s3p(^1P_1^o)$  of O VII. At these energies the core ion goes through an allowed transition, while the outer electron remains a ‘spectator’ in a doubly-excited resonance state, followed by

autoionization of the O VI resonance into the ground level of O VII. The effect gets more distinct for cross sections of higher excited levels. For low charge ions, PEC resonances are usually wider. These resonances in O VI depict the behavior of cross sections that determine corresponding features in level-specific recombination rates.

#### 4.1.2. *Recombination cross sections and rate coefficients*

The results consist of the total and 98 level-specific ( $n \leq 10$ ) recombination rate coefficients  $\alpha_R(T)$  and  $\alpha_i(T)$  respectively. Total recombination rates are given in Table 2. The main features are illustrated and compared with previously available data for RR and DR rates in Fig. 3. The solid curve is the BPRM total unified  $\alpha_R(T)$  and shows typical features. The high values at very low temperature are due to the dominance of RR into an infinity of high- $n$  levels.  $\alpha_R(T)$  decreases with increasing T until high temperatures where it rises due to the dominance of DR, followed by a monotonous decrease. The dotted curve in Fig. 3 is the total rate in LS couplig (Nahar 1999). The difference between the LS coupling  $\alpha_R(T)$  and the present BPRM rate is due to relativistic effects *and* radiation damping of low- $n$  resonances. Both effects can be important for highly charged ions. The dashed curve is the RR rate by Pequignot et al (1991) obtained by smoothing of OP data over resonances, and hydrogenic approximation. The agreement is good in the low region since non-resonant cross sections dominate the low energy region. The dot-dashed curve is the DR rate by Badnell et al. (1990) using the isolated resonance approximation. The sum of previous RR and DR rates agrees with the present unified rates to about 10-20%, as expected for highly charged ions.

The 98 level-specific recombination rate coefficients  $\alpha_i(T)$  for O VI are for  $i \equiv n(SLJ)$ ,  $n \leq 10$  and  $\ell \leq 9$ , and associated  $J\pi$  levels. Fig. 4 presents  $\alpha_i(T)$  into eight  $n = 2$  and 3 levels with  $n$  (SLJ):  $2s \ ^2S_0$ ,  $2p \ ^2P_{1/2,3/2}^o$ ,  $3s \ ^2S_0$ ,  $3p \ ^2P_{1/2,3/2}^o$ , and  $3d \ ^2D_{3/2,5/2}$ . These rates

are relatively smooth except for a small and diffuse DR ‘bump’. The levels correspond to the prominent 1032 and 1038 Å UV doublet lines respectively in O VI spectra arising due to strong dipole transitions  ${}^2P_{3/2,1/2}^o \longrightarrow {}^2S_{1/2}$ .

Total photorecombination cross sections  $\sigma_{RC}$  show features similar to photoionization cross sections  $\sigma_{PI}$  — smooth decay with energy, before the resonance complexes begin to emerge at high energies. However, ( $\sigma_{RC}$  are more complicated than  $\sigma_{PI}$  since all levels contribute to the total  $\sigma_{RC}$ , shown in Fig 5(a) for O VI. The resonance complexes are marked as KLL, KLM, KLN etc. For heavier high-Z elements than oxygen ( $Z > 10$ ) these manifest themselves as di-electronic satellite lines observed in tokamaks, Electron-Beam-Ion-Traps (EBIT), ion storage rings and astrophysical sources. The KLL complexes have been well studied in previous works (e.g. Gabriel 1972, Bely-Dubau et al. 1982, Pradhan and Zhang 1997, Zhang et al. 1999), Beiersdorfer et al. 1992, Oelgoetz and Pradhan 2001), for various ions.

## 4.2. O VII

### 4.2.1. Photoionization

Total and partial photoionization cross sections  $\sigma_{PI}$  for 116 levels  $n$  (SLJ) ( $n \leq 10$ ) are computed (the partial cross sections are for ionization into the ground level  $1s({}^2S_{1/2})$  of O VIII). Illustrative results are presented in Fig. 6. Fig. 6(a) shows the photoionization cross section of the ground level ( $1s^2 {}^1S_0$ ) of O VII. Similar to O VI, the Rydberg series of resonances, KL and  $Kn$  ( $n > 2$ ), begins at fairly high energies owing to the high  $n = 2$  excitation thresholds of O VIII. However, the ground level  $\sigma_{PI}$  of O VII does not show a significant K-shell jump at  $n = 2$  threshold, as seen in O VI. Nonetheless the feature is prominent in the excited  $n = 2$  level cross sections

as seen in Figs. 6(b)-(e). These excited levels are responsible for the formation of the important X-ray diagnostic lines, w, x, y, z, from the allowed and forbidden transitions  $1s^2 (^1S_0) \leftarrow 1s2p(^1P_1^o), 1s2p(^3P_2^o), 1s2p(^3P_1^o), 1s2s(^3S_1)$ , respectively. The K-shell ionization jump at the  $n = 2$  target levels

$$h\nu + O\ VII(1s2s, 1s2p) \longrightarrow e + O\ VIII(2s, 2p) .$$

can be seen clearly in the photoionization cross sections.

#### 4.2.2. *Recombination cross sections and rate coefficients*

Total recombination rate coefficients for O VII over a wide temperature range are presented in Table 3. In Fig. 7 the solid curve is the present total recombination rate coefficients, including relativistic effects in BPRM approximation and radiation damping of low- $n$  ( $n \leq 10$ ) resonances. The solid curve has the same general shape typical of unified recombination rates - the high rate at low temperature decreases until the recombination is dominated by DR forming a hump at high temperature. The dotted curve in the figure is the earlier total unified rate (Nahar 1999) where a part of the rates, the resonances  $2lnl$  converging on to the  $n = 2$  thresholds of O VIII, were also computed using the BPRM method including radiation damping (Zhang et al. 1999); the remainder was in LS coupling. Both results show very close agreement since the main  $n = 2$  resonant contributions are the same. However, present rates also include  $n = 3, 4$  resonant contributions  $3lnl, 4lnl$ . The dashed curve is the RR rate obtained by Verner and Ferland (1996), which agrees well with the present one in the region where DR is small. The dot-dashed curve is the DR rate calculated by Savin (1999) from experimentally measured recombination cross sections by Wolf et al. (1991). As is discernible from Fig. 7, the sum of the previous RR and the experimental DR rates (RR+DR) is significantly lower than the present unified rate



for O VII. At the temperature of peak DR contribution  $\text{Log } T = 6.6$ , the unified rate is about 20% higher the RR+DR value. This is most likely because the experimental DR measurements cover a smaller energy range and do not include all contributions.

Level-specific recombination rate coefficients are obtained for 116 levels  $n$  (SLJ) with  $0 \leq J \leq 4$  and  $n \leq 10$ . These rates for fine structure levels were not obtained in our earlier work (Nahar 1999). Fig. 8 presents level specific rates for the  $n = 2$  levels corresponding to the X-ray w, x, y, and z lines of O VII. The rates show a relatively smooth decay with temperature except for the high temperature DR bump for  $1s2p(^1P_1^o)$  and  $1s2s(^3S_1)$  levels.

The total recombination cross sections  $\sigma_{RC}$ , summed over recombination cross sections of individual fine structure levels up to  $n = 10$  of O VII and high- $n$  contributions are presented in Fig. 5(b). The resonance complexes LL, LM, LN, MM etc. of  $n = 2$  and 3 thresholds of the core are specified in the figure. The  $n = 4$  resonances are too low for any significant contributions. These complexes are seen at high energies near the high lying O VIII thresholds.

As mentioned above, as a numerical check on the calculations we verify that the sum of the level-specific rate coefficients and the DR contribution agrees within a few percent with the total recombination rate coefficient obtained from total collision strengths obtained from  $\sigma_{RC}$  in Fig. 5 for both O VI and O VII.

#### 4.2.3. Ionization fractions in coronal equilibrium

Using the present total unified recombination rates,  $\alpha_R(T)$ , for O VI and O VII we calculate ionization fractions of oxygen ions in coronal (collisional) equilibrium,

$$N(z-1, g)S(z-1, g) = N(z, g)\alpha(z, g), 1 \leq z \leq z_{max}, \quad (11)$$

where  $S$  is the rate coefficient for electron impact ionization and total element density  $N_T = \sum_{z=0}^{z_{max}} N(z, g)$ . The ionization fractions in  $-\log[N(z)/N_T]$  are given in Table 3. However, present fractions show very little difference from earlier values (Nahar 1999). Most of the differences are in the third significant digit and do not show up in Table 3.

## 5. CONCLUSION

Extensive results from relativistic calculations for total and level-specific photoionization and recombination cross sections and rates are presented for O VI and O VII. These are of general interest in UV and X-ray spectroscopy of laboratory and astrophysical sources, especially the formation due to recombination of important lines such as the  $\lambda\lambda$  1032,1038 fine structure doublet in O VI, and the ‘triplet’ X-ray features in O VII.

A discussion of some of the important atomic effects such as resolution and radiation damping of resonances, interference between non-resonant (RR) and resonant (DR) recombination, comparison with experimental data and uncertainties, and general features of the unified (e + ion) recombination rates, has also been given in the first paper on the new BPRM calculations – paper IV in the present series (Nahar et al. 2000).

Di-electronic satellite rates for the KLL, KLM, etc, complexes of several ions have earlier been shown to be in very good agreement with experiments and other theoretical calculations (Pradhan and Zhang 1997; Zhang et al. 1999), to about 10-20%; it is therefore expected that the present rates should be definitive, with similar uncertainties.

The present level-specific data can be used to construct recombination-cascade matrices for O VI and O VII, to obtain effective recombination rates into specific fine structure levels  $n$  (SLJ) with  $n \leq 10$  and  $\ell \leq n - 1$  (e.g. Pradhan 1985). The present data is more than sufficient for extrapolation to high- $n, \ell$  necessary to account for all cascade contributions.

The available data includes: (A) Photoionization cross sections, both total and partial, for bound fine structure levels of O VI and O VII up to the  $n = 10$  levels. (B) Total unified recombination rates for O VI and O VII, and level-specific recombination rate coefficients for levels up to  $n = 10$ . Further calculations for other He-like and Li-like ions are in progress. All photoionization and recombination data are available electronically at: [nahar@astronomy.ohio-state.edu](mailto:nahar@astronomy.ohio-state.edu). The total recombination rate coefficients are also available from the Ohio State Atomic Astrophysics website at: [www.astronomy.ohio-state.edu/~pradhan](http://www.astronomy.ohio-state.edu/~pradhan).

This work was supported partially by NSF and NASA. The computational work was carried out on the Cray SV1 at the Ohio Supercomputer Center in Columbus, Ohio.

Table 1: Target levels in the eigenfunction expansions of O VII and O VIII.

O VI			O VIII		
level	$E_t(Ry)$		level	$E_t(Ry)$	
1	1s <sup>2</sup> ( <sup>1</sup> S <sub>0</sub> )	0.0	1	1s( <sup>2</sup> S <sub>1/2</sub> )	0.00
2	1s2s( <sup>3</sup> S <sub>1</sub> )	41.232	2	2p( <sup>2</sup> P <sub>1/2</sub> <sup>o</sup> )	48.0308997
3	1s2p( <sup>3</sup> P <sub>0</sub> <sup>o</sup> )	41.787	3	2s( <sup>2</sup> S <sub>1/2</sub> )	48.0315698
4	1s2p( <sup>3</sup> P <sub>1</sub> <sup>o</sup> )	41.788	4	2p( <sup>2</sup> P <sub>3/2</sub> <sup>o</sup> )	48.0445917
5	1s2p( <sup>3</sup> P <sub>2</sub> <sup>o</sup> )	41.793	5	3p( <sup>2</sup> P <sub>1/2</sub> <sup>o</sup> )	56.9304970
6	1s2s( <sup>1</sup> S <sub>0</sub> )	41.812	6	3s( <sup>2</sup> S <sub>1/2</sub> )	56.9306973
7	1s2p( <sup>1</sup> P <sub>1</sub> <sup>o</sup> )	42.184	7	3d( <sup>2</sup> D <sub>1/2</sub> )	56.9345473
8	1s3s( <sup>3</sup> S <sub>1</sub> )	48.651	8	3p( <sup>2</sup> P <sub>3/2</sub> <sup>o</sup> )	56.9345541
9	1s3p( <sup>3</sup> P <sub>0</sub> )	48.804	9	3d( <sup>2</sup> D <sub>5/2</sub> )	56.9358976
10	1s3p( <sup>3</sup> P <sub>1</sub> <sup>o</sup> )	48.804	10	4p( <sup>2</sup> P <sub>1/2</sub> <sup>o</sup> )	60.0447993
11	1s3p( <sup>3</sup> P <sub>2</sub> <sup>o</sup> )	48.804	11	4s( <sup>2</sup> S <sub>1/2</sub> )	60.0448841
12	1s3s( <sup>1</sup> S <sub>0</sub> )	48.811	12	4d( <sup>2</sup> D <sub>3/2</sub> )	60.0465078
13	1s3d( <sup>3</sup> D <sub>3</sub> )	48.884	13	4p( <sup>2</sup> P <sub>3/2</sub> <sup>o</sup> )	60.0465108
14	1s3d( <sup>3</sup> D <sub>2</sub> )	48.884	14	4f( <sup>2</sup> P <sub>5/2</sub> <sup>o</sup> )	60.0470765
15	1s3d( <sup>3</sup> D <sub>1</sub> )	48.884	15	4d( <sup>2</sup> D <sub>5/2</sub> )	60.0470775
16	1s3d( <sup>1</sup> D <sub>1</sub> )	48.894	16	4f( <sup>2</sup> P <sub>7/2</sub> <sup>o</sup> )	60.0473612
17	1s3p( <sup>1</sup> P <sub>1</sub> <sup>o</sup> )	48.922			

O VII: Correlations - 2s<sup>2</sup>, 2p<sup>2</sup>, 3s<sup>2</sup>, 3p<sup>2</sup>, 3d<sup>2</sup>, 2s2p, 2s3s,  
2s3p, 2s3d, 2s4s, 2s4p, 2p3s, 2p3p, 2p3d, 2p4s, 2p4p,  
 $\lambda_{nl}$  - 0.991(1s), 0.991(2s), 0.776(2p), 1.16883(3s), 0.91077(3p),  
1.00746(3d), -1.59699(4s), -1.61237(4p) — see text)

O VIII:  $\lambda_{nl}$  - 1.0, for 1s to 4f

Table 2: Total recombination rate coefficients  $\alpha_R(T)$  for O VI, O VII and O VIII.

$\log_{10}T$		$\alpha_R(\text{cm}^3\text{s}^{-1})$		$\log_{10}T$		$\alpha_R(\text{cm}^3\text{s}^{-1})$	
(K)	O VI	O VII	O VIII	(K)	O VI	O VII	O VIII
1.0	1.42E-09	1.99E-09	2.90E-09	5.1	3.72E-12	6.16E-12	1.03E-11
1.1	1.25E-09	1.76E-09	2.56E-09	5.2	3.13E-12	5.28E-12	8.78E-12
1.2	1.10E-09	1.55E-09	2.26E-09	5.3	2.62E-12	4.51E-12	7.51E-12
1.3	9.68E-10	1.36E-09	2.00E-09	5.4	2.19E-12	3.85E-12	6.42E-12
1.4	8.50E-10	1.20E-09	1.76E-09	5.5	1.83E-12	3.28E-12	5.48E-12
1.5	7.46E-10	1.05E-09	1.55E-09	5.6	1.52E-12	2.79E-12	4.67E-12
1.6	6.53E-10	9.23E-10	1.36E-09	5.7	1.26E-12	2.37E-12	3.97E-12
1.7	5.72E-10	8.10E-10	1.20E-09	5.8	1.05E-12	2.01E-12	3.37E-12
1.8	5.01E-10	7.10E-10	1.05E-09	5.9	8.99E-13	1.72E-12	2.85E-12
1.9	4.38E-10	6.21E-10	9.26E-10	6.0	8.42E-13	1.52E-12	2.40E-12
2.0	3.83E-10	5.44E-10	8.12E-10	6.1	9.14E-13	1.44E-12	2.03E-12
2.1	3.34E-10	4.75E-10	7.12E-10	6.2	1.11E-12	1.52E-12	1.71E-12
2.2	2.91E-10	4.15E-10	6.23E-10	6.3	1.39E-12	1.73E-12	1.43E-12
2.3	2.54E-10	3.62E-10	5.46E-10	6.4	1.65E-12	1.99E-12	1.20E-12
2.4	2.21E-10	3.16E-10	4.78E-10	6.5	1.82E-12	2.21E-12	9.96E-13
2.5	1.93E-10	2.76E-10	4.18E-10	6.6	1.86E-12	2.31E-12	8.27E-13
2.6	1.67E-10	2.40E-10	3.65E-10	6.7	1.78E-12	2.26E-12	6.84E-13
2.7	1.46E-10	2.09E-10	3.19E-10	6.8	1.60E-12	2.10E-12	5.63E-13
2.8	1.27E-10	1.82E-10	2.78E-10	6.9	1.38E-12	1.85E-12	4.61E-13
2.9	1.10E-10	1.58E-10	2.43E-10	7.0	1.14E-12	1.56E-12	3.75E-13
3.0	9.52E-11	1.37E-10	2.12E-10	7.1	9.19E-13	1.28E-12	3.05E-13
3.1	8.25E-11	1.19E-10	1.85E-10	7.2	7.20E-13	1.02E-12	2.45E-13
3.2	7.15E-11	1.03E-10	1.61E-10	7.3	5.54E-13	7.96E-13	1.96E-13
3.3	6.19E-11	8.97E-11	1.40E-10	7.4	4.19E-13	6.10E-13	1.57E-13
3.4	5.35E-11	7.77E-11	1.22E-10	7.5	3.13E-13	4.61E-13	1.24E-13
3.5	4.62E-11	6.73E-11	1.06E-10	7.6	2.32E-13	3.45E-13	9.76E-14
3.6	3.99E-11	5.82E-11	9.22E-11	7.7	1.70E-13	2.56E-13	7.63E-14
3.7	3.43E-11	5.04E-11	8.01E-11	7.8	1.24E-13	1.89E-13	5.93E-14
3.8	2.96E-11	4.35E-11	6.95E-11	7.9	9.00E-14	1.38E-13	4.59E-14
3.9	2.54E-11	3.76E-11	6.03E-11	8.0	6.50E-14	1.01E-13	3.51E-14
4.0	2.18E-11	3.25E-11	5.22E-11	8.1	4.69E-14	7.35E-14	2.70E-14
4.1	1.87E-11	2.80E-11	4.53E-11	8.2	3.37E-14	5.33E-14	2.05E-14
4.2	1.61E-11	2.41E-11	3.92E-11	8.3	2.42E-14	3.86E-14	1.55E-14
4.3	1.37E-11	2.08E-11	3.39E-11	8.4	1.73E-14	2.79E-14	1.16E-14
4.4	1.17E-11	1.79E-11	2.93E-11	8.5	1.24E-14	2.02E-14	8.72E-15
4.5	1.00E-11	1.54E-11	2.53E-11	8.6	8.87E-15	1.45E-14	6.51E-15
4.6	8.54E-12	1.32E-11	2.18E-11	8.7	6.33E-15	1.05E-14	4.83E-15
4.7	7.26E-12	1.14E-11	1.88E-11	8.8	4.52E-15	7.55E-15	3.58E-15
4.8	6.16E-12	9.77E-12	1.62E-11	8.9	3.23E-15	5.44E-15	2.64E-15
4.9	5.22E-12	8.38E-12	1.39E-11	9.0	2.30E-15	3.91E-15	1.93E-15
5.0	4.41E-12	7.20E-12	1.19E-11				

Table 3: Ionization fractions,  $-\log_{10} \frac{N(z)}{N_T}$ , of oxygen ions in coronal equilibrium.

$\log_{10} T$	$-\log_{10} N(z)/N_T$								
	O I	O II	O III	O IV	O V	O VI	O VII	O VIII	O IX
4.0	0.001	2.5	*****	*****	*****	*****	*****	*****	*****
4.1	0.0433	1.02	*****	*****	*****	*****	*****	*****	*****
4.2	0.432	0.2	7.91	*****	*****	*****	*****	*****	*****
4.3	1.19	0.029	5.37	*****	*****	*****	*****	*****	*****
4.4	1.77	0.008	3.49	*****	*****	*****	*****	*****	*****
4.5	2.12	0.007	2.10	8.15	*****	*****	*****	*****	*****
4.6	2.38	0.037	1.11	5.38	*****	*****	*****	*****	*****
4.7	2.72	0.176	0.481	3.39	9.73	*****	*****	*****	*****
4.8	3.21	0.483	0.179	2.05	6.89	*****	*****	*****	*****
4.9	3.82	0.901	0.096	1.14	4.76	*****	*****	*****	*****
5.0	4.52	1.40	0.174	0.539	3.17	7.54	*****	*****	*****
5.1	5.33	2.01	0.417	0.23	2.02	5.13	8.58	*****	*****
5.2	6.22	2.71	0.778	0.114	1.21	3.28	5.48	*****	*****
5.3	7.16	3.45	1.22	0.155	0.646	1.87	3.04	*****	*****
5.4	8.23	4.32	1.82	0.41	0.387	0.895	1.23	*****	*****
5.5	9.78	5.67	2.92	1.20	0.724	0.634	0.289	*****	*****
5.6	*****	7.43	4.43	2.43	1.57	0.975	0.064	8.40	*****
5.7	*****	9.11	5.89	3.64	2.43	1.40	0.019	6.32	*****
5.8	*****	*****	7.19	4.71	3.18	1.78	0.007	4.66	*****
5.9	*****	*****	8.33	5.63	3.82	2.10	0.004	3.31	7.86
6.0	*****	*****	9.31	6.41	4.34	2.34	0.005	2.23	5.52
6.1	*****	*****	*****	7.05	4.75	2.49	0.020	1.39	3.66
6.2	*****	*****	*****	7.61	5.09	2.60	0.080	0.795	2.24
6.3	*****	*****	*****	8.19	5.47	2.76	0.231	0.455	1.22
6.4	*****	*****	*****	8.89	5.98	3.08	0.527	0.368	0.56
6.5	*****	*****	*****	9.74	6.65	3.56	0.984	0.51	0.231
6.6	*****	*****	*****	*****	7.41	4.15	1.52	0.77	0.096
6.7	*****	*****	*****	*****	8.16	4.75	2.05	1.06	0.044
6.8	*****	*****	*****	*****	8.90	5.33	2.55	1.33	0.022
6.9	*****	*****	*****	*****	9.59	5.88	3.00	1.57	0.012
7.0	*****	*****	*****	*****	*****	6.41	3.42	1.79	0.007
7.1	*****	*****	*****	*****	*****	6.91	3.81	1.98	0.005
7.2	*****	*****	*****	*****	*****	7.39	4.17	2.16	0.003
7.3	*****	*****	*****	*****	*****	7.85	4.50	2.32	0.002
7.4	*****	*****	*****	*****	*****	8.28	4.82	2.47	0.001
7.5	*****	*****	*****	*****	*****	8.70	5.12	2.61	0.001

## REFERENCES

- Arav, N., Kaastra, J., Steenbrugge, K., Brinkman, B., Edelson, R., Korista, K.T., de Kool, M. 2003, ApJ (submitted, astro-ph/0303425).
- Atomic data needs in X-ray astronomy*, Eds. M.A. Bautista, T. R. Kallman, A.K. Pradhan, 2000, NASA Publications NASA/CP-2000-209968, ADXA, (<http://heasarc.gsfc.nasa.gov/docs/heasarc/atomic/proceed.html>)
- Badnell N R, Pindzola M S and Griffin D C 1990 Physical Review A **41** 2422
- Bell, R.H. & Seaton, M.J. 1985, J. Phys. B 18, 1589
- Bely-Dubau, F., Dubau, J., Faucher, P. & Gabriel, A.H. 1982, Mon. Not. R. Roy. Astro. Soc. 198, 239
- Beiersdorfer, P., Schneider, M. B., Bitter, M. & von Goeler, S. 1992, Rev Sci Instrum. 63, 5029
- Berrington, K. A., Burke, P.G., Butler, K., Seaton, M.J., Storey, P.J., Taylor, K.T. & Yu Yan 1987, J. Phys. B 20, 6379
- Berrington, K.A., Eissner, W., Norrington, P.H. 1995, Comput. Phys. Commun. 92, 290
- Cen, R., Tripp, T.M., Ostriker, J.P., & Jenkins, E.B. 2001, ApJ, 559, 5
- Eissner, W., Jones, M., & Nussbaumer, H. 1974, Comput. Phys. Commun. 8, 270
- Fang, T. & Canizares, C.R. 2000, ApJ, 532, 539
- Gabriel, A.H. 1972, Mon. Not. R. astr. Soc. 1972, 160, 99
- Hummer, D.G., Berrington, K.A., Eissner, W., Pradhan, A.K., Saraph, H.E., & Tully, J.A. 1993, Astron. Astrophys. 279, 298

- Kaastra, J.S., Mewe, R., Liedahl, D.A., Komossa, S., Brinkman, A.C., 2000, *Astron. Astrophys.* 83, 354L
- Nahar, S.N. 1996, *Phys. Rev. A* 53, 2417
- Nahar, S.N. 1998, *Phys. Rev. A* 58, 3766
- Nahar, S.N. 1999, *ApJS* 120, 131
- Nahar, S.N., & Pradhan, A.K. 1992, *Phys. Rev. Lett.* 68, 1488
- Nahar, S.N., & Pradhan, A.K. 1994, *Phys. Rev. A* 49, 1816
- Nahar, S.N., & Pradhan, A.K. 1997, *ApJS* 111, 339
- Nahar, S.N., Pradhan, A.K. & Zhang, H.L. 2000, *ApJS* 131, 375
- Nahar, S.N., Pradhan, A.K. & Zhang, H.L. 2001, *ApJS* 133, 255
- NIST compiled database, [www.nist.gov](http://www.nist.gov)
- Oelgoetz, J. & Pradhan A.K. 2001, *MNRAS* 327, L42
- Pequignot, D., Petitjean, P., & Boisson, C. 1991, *Astron. Astrophys.* 251, 680
- Pradhan, A.K. 1985, *Astrophys. J.* 284, 824
- Pradhan, A.K. 2000, *Astrophys. J. (Letters)* 545 L165
- Pradhan, A.K. and Zhang, H. L. 1997, *J. Phys. B* 30, L571
- Sakimoto K., Terao M., & Berrington K.A. 1990, *Phys. Rev. A* 42, 291
- Savin, D.W. 1999, *ApJ.* 523, 855
- Scott N.S. & Burke P.G. 1980, *J. Phys. B* 12, 4299



Scott N.S. & Taylor K.T. 1982, *Comput. Phys. Commun.* 25, 347

Seaton, M.J. 1987, *J. Phys. B* 20, 6363

*The Opacity Project 1 & 2*, 1995, 1996, compiled by the Opacity Project team (Institute of Physics Publishing, Bristol and Philadelphia)

Verner, D.A. & Ferland G. 1996, *ApJS*. 103, 467

Wolf A, Berger J, Bock M, Habs D, Hochadel B, Kilgus G, Neureither G, Schramm U, Schwalm D, Szmola E, Müller A, Waner M, and Schuch R 1991 *Z. Phys. D Suppl.* 21, 569

Yoshikawa, K., Yamasaki, N.Y., Suto, Y., Ohashi, T., Mitsuda, K., Tawara, Y., Furuzawa, Y. 2003, *ApJ* (submitted, astro-ph/0303281)

Zhang, H.L., Nahar, S.N. & Pradhan, A.K. 1999, *J. Phys. B*, 32. 1459

Zhang, H.L. & Pradhan, A.K. 1997, *Physical Review Letters* 78, 195

Zhang, H.L. & Pradhan, A.K. 1997, *J. Phys. B* 30, L571

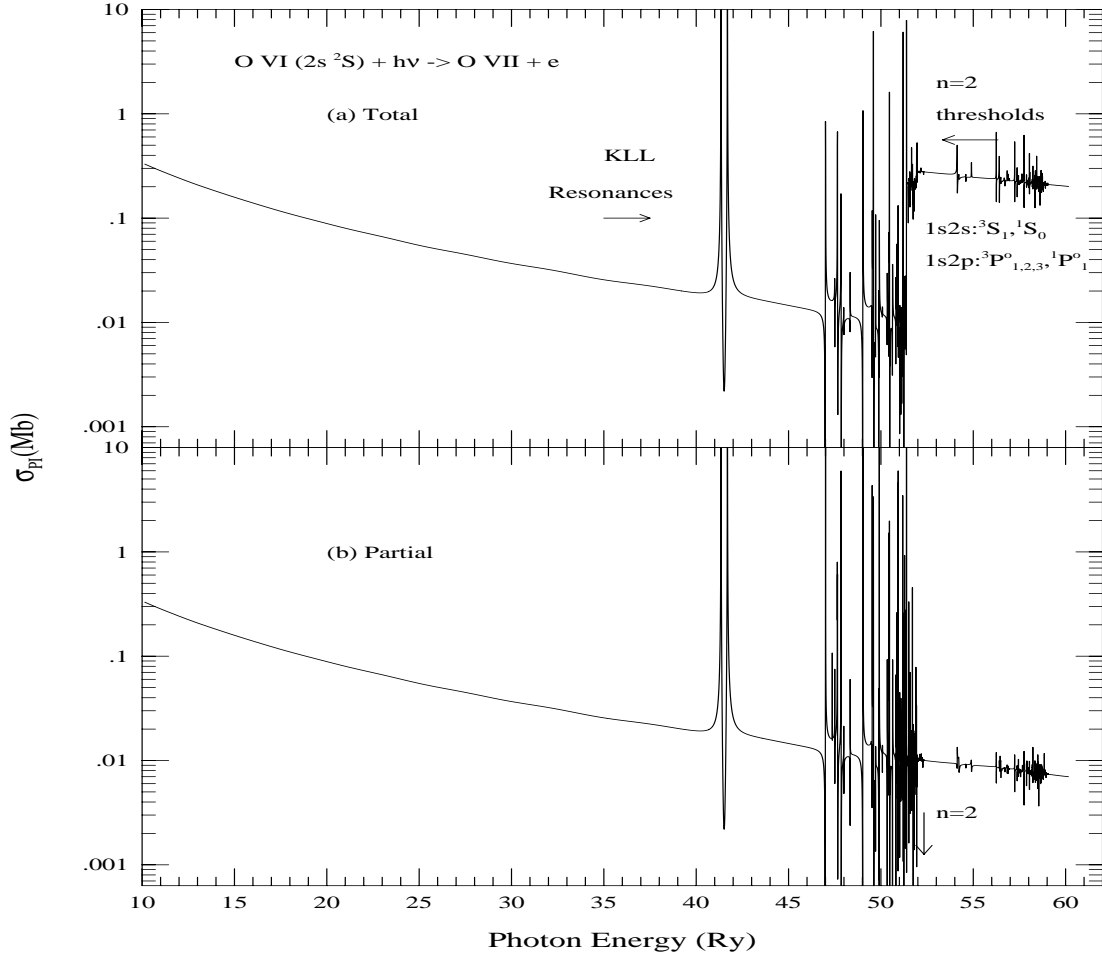


Fig. 1.— Photoionization cross sections of the ground level  $1s^2\ 2s\ (^2S_{1/2})$  of O VI: (a) Total cross section; the large jump around 52 Ry corresponds to the  $n=2$  K-shell ionization edge. (b) Partial cross section into the ground level  $1s^2\ (^1S_0)$  of O VII; note that the jump is no longer present and the cross section is continuous across the  $n = 2$  thresholds of O VII.

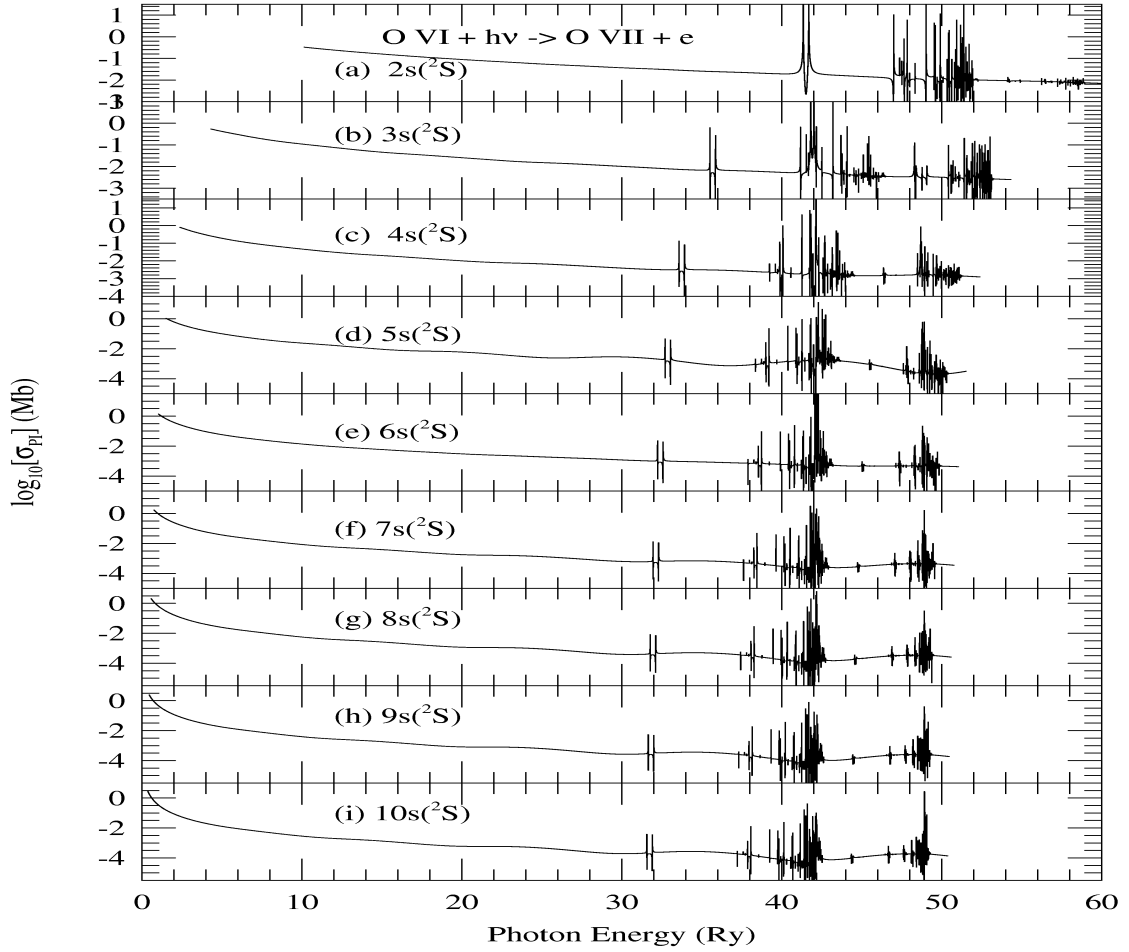


Fig. 2.— Partial photoionization cross sections of the Rydberg series of levels  $1s^2ns(2S_{1/2})$  of O VI into the ground state state  $1s^2(1S_0)$  of O VII. *photoexcitation-of-core* (PEC) resonances are seen at about 42 and 49 Ry.

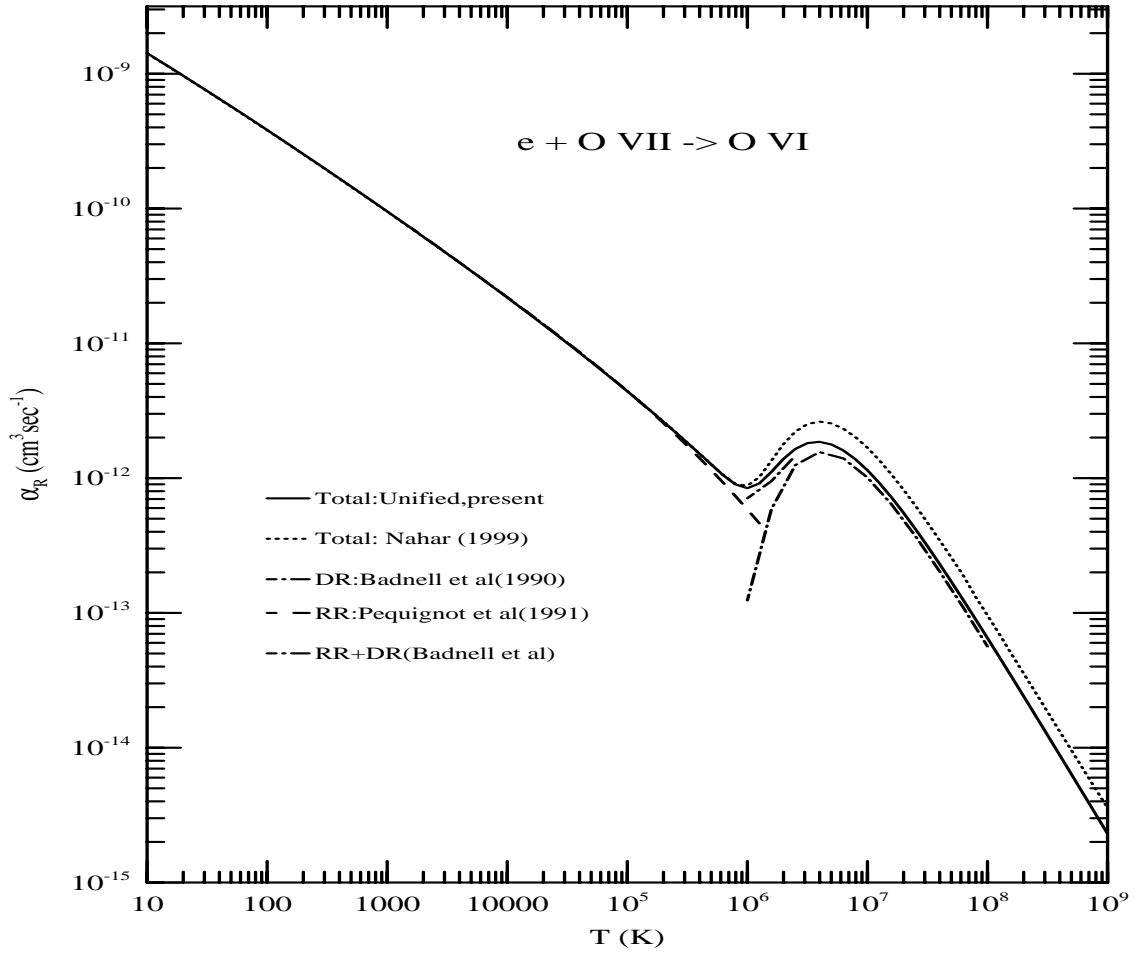


Fig. 3.— Total unified recombination rate coefficients for O VI: BPRM with fine structure (solid curve); Total in LS coupling (Nahar 1999, dotted); RR rates by Pequignot et al (1991, dash), DR rates by Badnell et al. (1990, dot-dash).

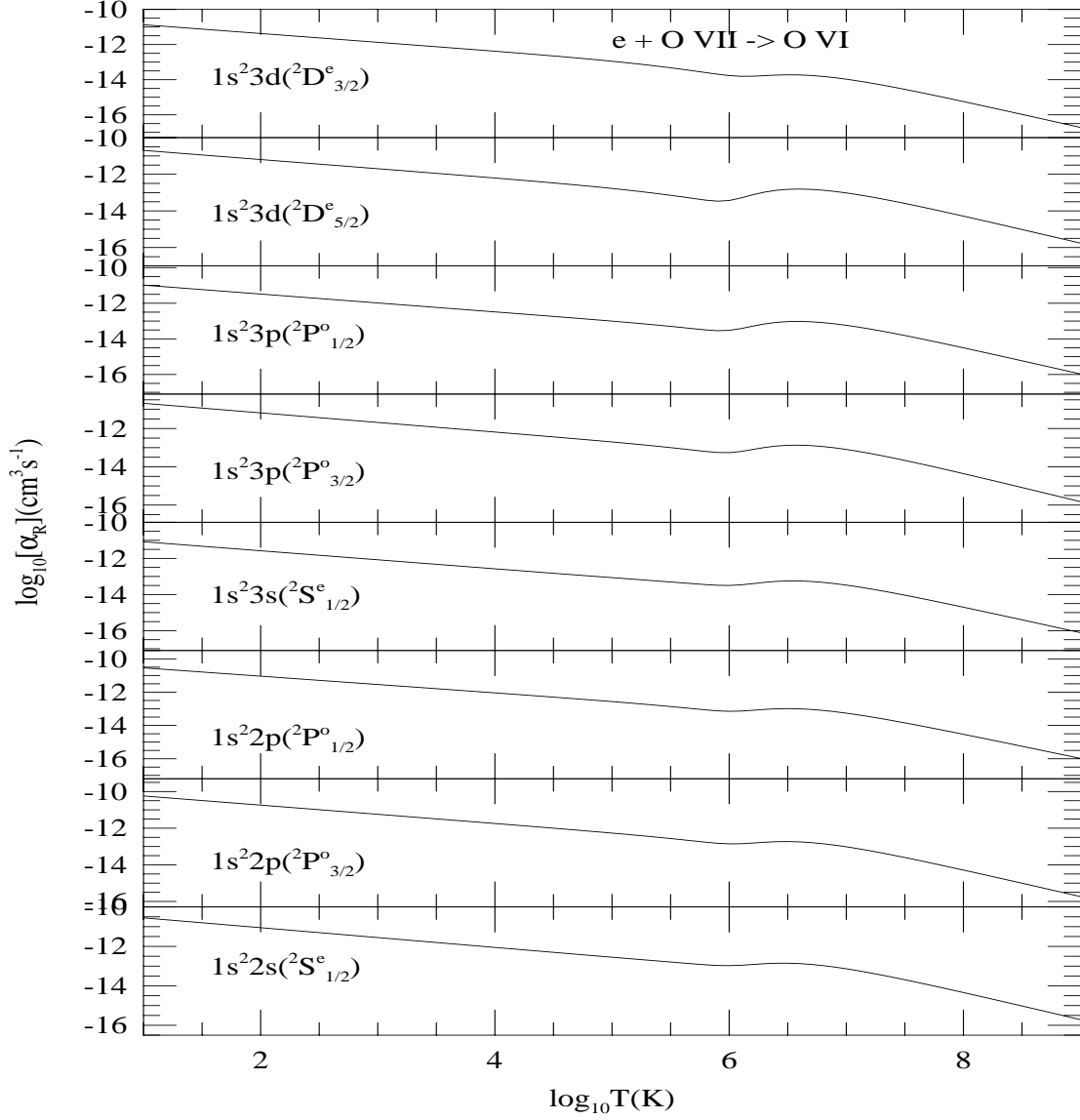


Fig. 4.— Level-specific recombination rate coefficients for O VI recombining to ground and excited  $n=2, 3$  levels. The strong dipole transitions  $^2P^o_{3/2,1/2} \rightarrow ^2S_{1/2}$  are responsible for the prominent 1032 and 1038 Å UV doublet lines respectively in O VI spectra.

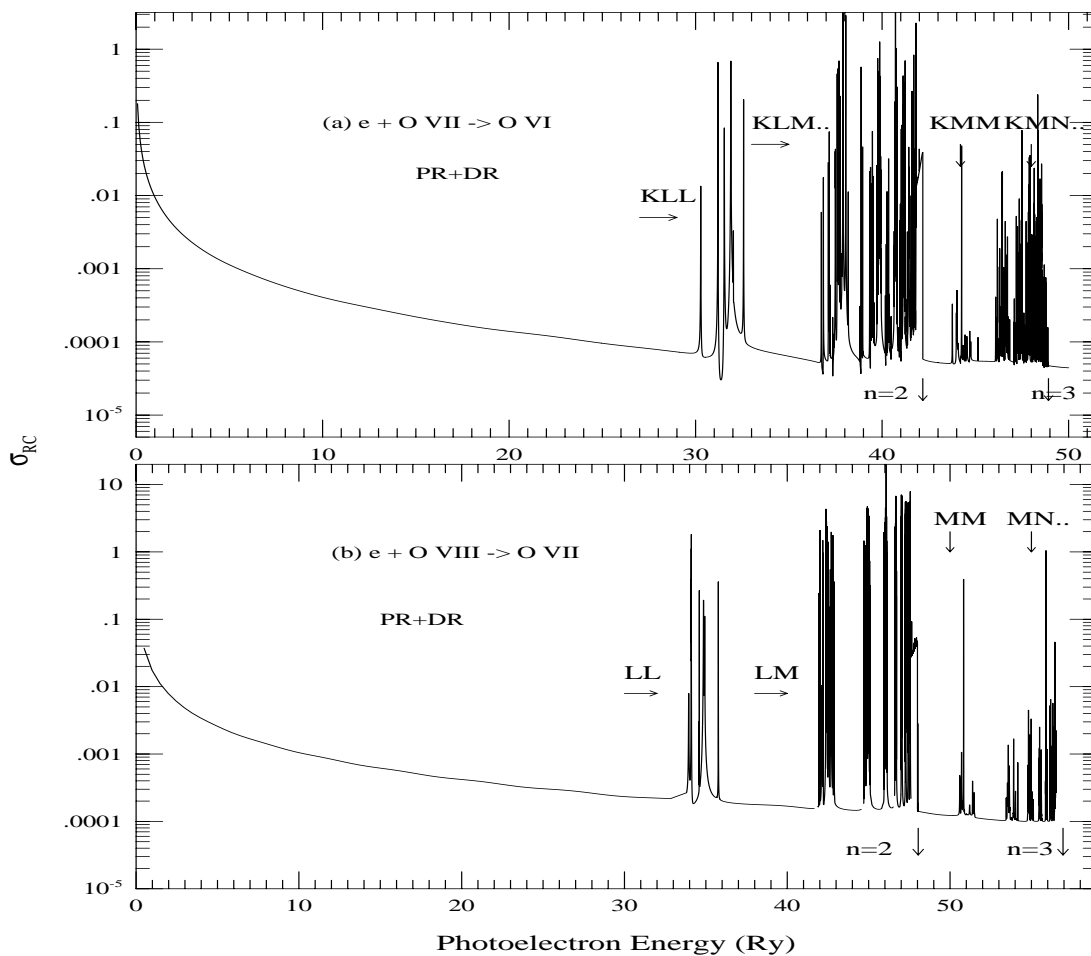


Fig. 5.— Total unified (e + ion) photo-recombination cross sections,  $\sigma_{RC}$ , of (a) O VI and (b) O VII. Note that the  $\sigma_{RC}$  exhibit considerably more resonance structures than the corresponding ground level  $\sigma_{PI}$  in Figs. 1 and 6, since the former are summed over the ground *and* many excited recombined levels.

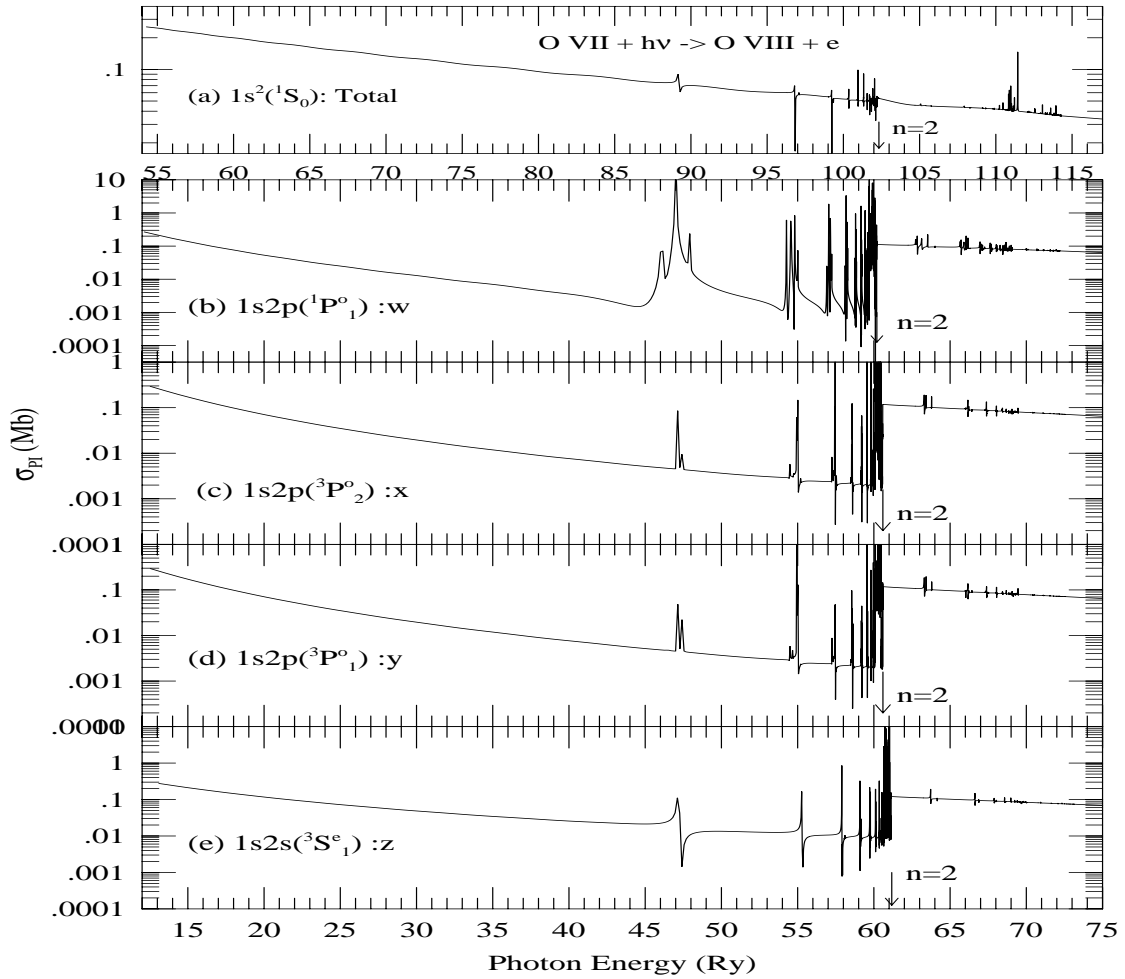


Fig. 6.— Level-specific photoionization cross sections of (a) the ground level  $1s^2 ({}^1S_0)$ , and (b) - (e) excited  $1s2s$  and  $1s2p$  levels of O VII responsible for the prominent X-ray lines: resonance (w), intercombination (x,y), and forbidden(z).

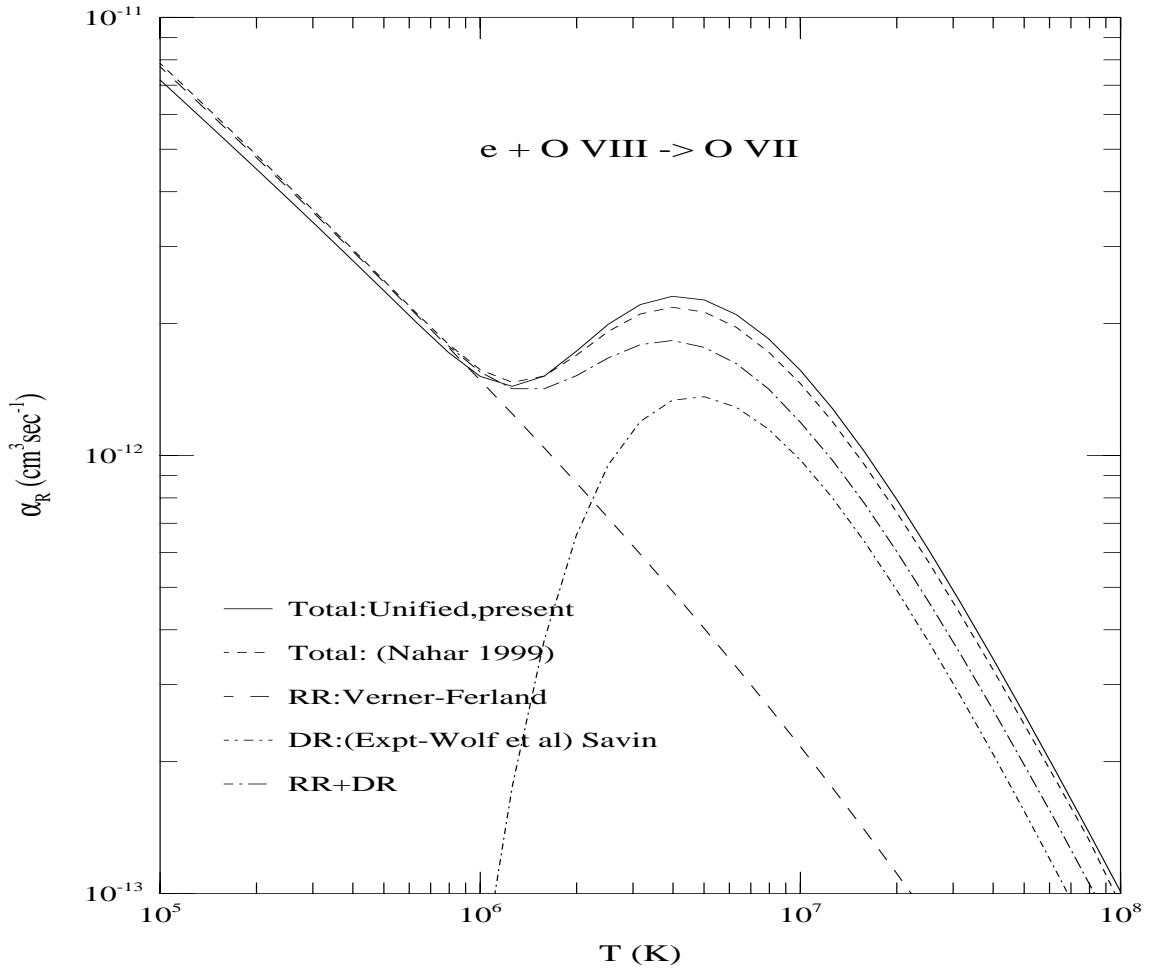


Fig. 7.— Total unified recombination rate coefficients for O VII: present BPRM (solid); total (dotted, Nahar 1999), RR rates by Verner and Ferland (1996) (dashed), DR rates by Savin (1999) from measured cross sections by Wolf et al. (1991) (dot-dashed).



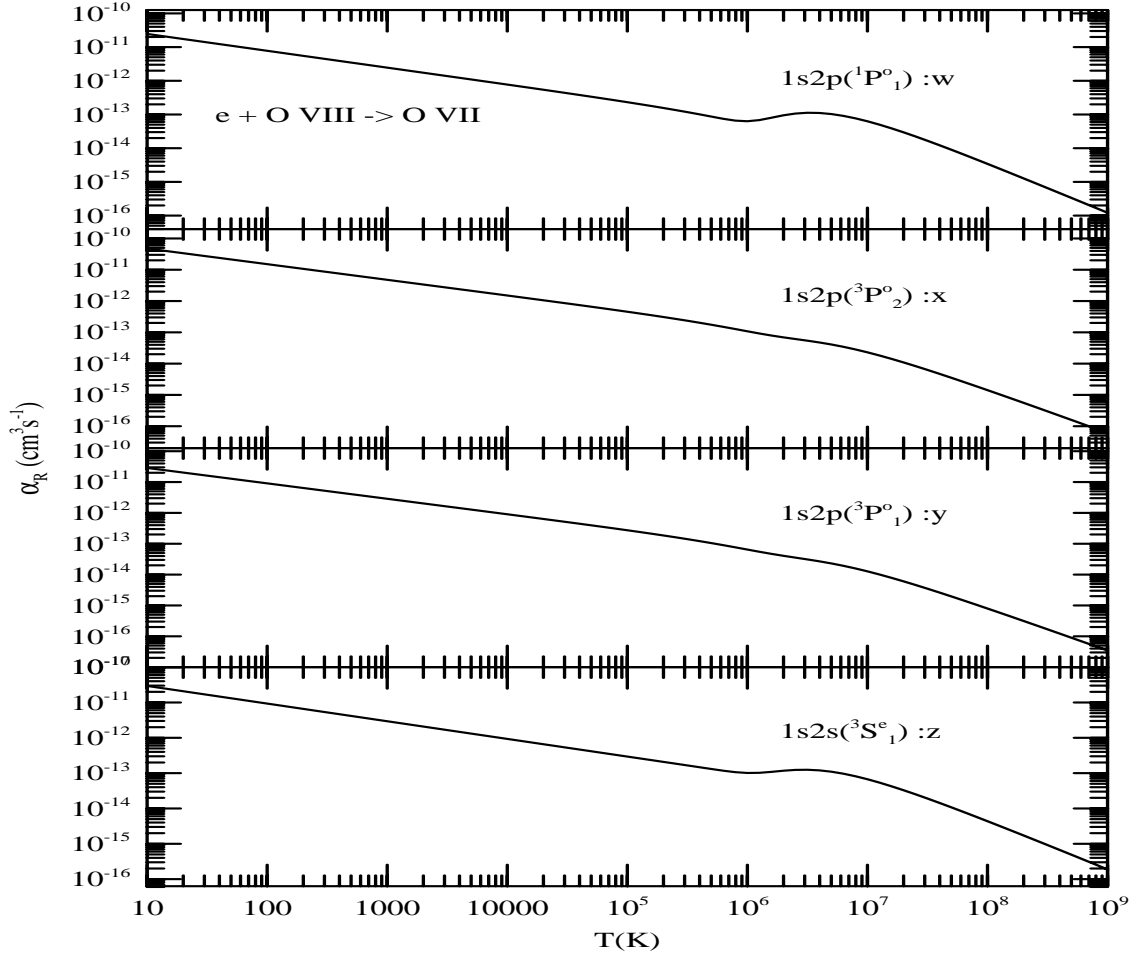


Fig. 8.— Level-specific recombination rate coefficients for O VII into the excited  $n = 2$  levels responsible for the prominent X-ray lines w, x, y, and z.